Cenozoic and Mesozoic metamorphism in the Longmenshan orogen: Implications for geodynamic models of eastern Tibet

Simon Wallis Department of Earth and Planetary Sciences, Graduate School of Environmental Studies, Nagoya University, Nagoya 464-8602, Japan
Tatsuki Tsujimori Research Institute of Natural Sciences, Okayama University of Science, Okayama 700-0005, Japan
Mutsuki Aoya Department of Earth and Planetary Sciences, Graduate School of Environmental Studies, Nagoya University, Nagoya 464-8602, Japan
Tetsuo Kawakami Department of Earth Sciences, Faculty of Education, Okayama University, Okayama 700-8530, Japan
Kentaro Terada Department of Earth and Planetary Systems Science, Graduate School of Science, Hiroshima University, Hiroshima 739-8526, Japan
Kazuhiro Suzuki Nagoya University Center for Chronological Research, Nagoya University, Nagoya 464-8602, Japan
Hironobu Hyodo Research Institute of Natural Sciences, Okayama University of Science, Okayama 700-0005, Japan

ABSTRACT

New zircon U-Pb and mica $^{40}Ar/^{39}Ar$ dating combined with structural studies in the Longmenshan orogen confirm that most of the upper crustal deformation in the eastern margin of Tibet is Mesozoic. However, at lower structural levels, apatite U-Pb and monazite electron microprobe dating reveals a previously unknown domain of Cenozoic (ca. 65 Ma) Barrovian-type metamorphism and deformation. This discovery shows that the crust in the eastern margin of Tibet was already a substantial thickness around the time of the India-Asia collision. Associated deformation has a N-S-oriented stretching lineation, implying that deformation was not driven by topographic gradients in the Tibetan Plateau. The observed moderate amounts of distributed postmetamorphic E-W shortening can probably explain the present thickness of the continental crust in the area. These results do not support models of crustal thickening caused by solid-state lateral flow of midcrustal metamorphic rocks.

Keywords: Tibetan Plateau, radiometric dating, metamorphism, Cenozoic tectonics.

INTRODUCTION

Despite its great elevation, the Tibetan Plateau is remarkably flat (e.g., Fielding et al., 1994). It is generally thought that the lack of great relief is due to the compensating flow of highly mobile midcrustal metamorphic rocks (e.g., Royden et al., 1997). This proposal has lead to a radical new idea in continental tectonics that horizontal outflow of mobile midcrustal rock from topographic highs is one of the principal mechanisms by which plateaus grow laterally (Royden et al., 1997). The best case for such a mechanism is made in the eastern border of Tibet in the Longmenshan. The Longmenshan is a region of relatively thick continental crust (Holt and Wallace, 1990), high elevation, and intense upper crustal deformation (Dirks et al., 1994; Burchfiel et al., 1995; Hou et al., 1995) with clear geomorphological continuity with the rest of the Tibetan Plateau (Clark and Royden, 2000). However, a number of studies have emphasized that the upper crustal deformation in the Longmenshan is almost entirely Mesozoic (Dirks et al., 1994; Burchfiel et al., 1995) and, therefore, unrelated to the India-Asia collision, which began ca. 54 Ma (Rowley, 1996). To explain this discrepancy, Royden et al. (1997) proposed that crustal thickening in the Longmenshan was caused by solid-state inflow of mobile midcrustal metamorphic rocks from a topographic high. This proposal is compatible with recent radiometric dating suggesting that the high relief is younger than 12 Ma (Kirby et al., 2002).

To test this model we use zircon and apatite U-Pb, monazite U-Th-Pb, and muscovite and biotite $^{40}Ar/^{39}Ar$ dating in combination with structural and petrographic observations to constrain the ages of deformation and metamorphism in central Longmenshan. We demonstrate the existence of a previously unknown region of ca. 65 Ma Barrovian-type metamorphism, implying that the Longmenshan crust was already thick at the time of the India-Asia collision and that only minor postcollisional deformation is needed to account for the present thickness.

METAMORPHISM AND DEFORMATION IN THE DANBA REGION

The Longmenshan consists of Triassic flysch and older sediments deposited on the western fringe of the Proterozoic Yangtze craton. This sequence has undergone strong subhorizontal shortening to form a major cleaved fold and thrust belt (Dirks et al., 1994; Burchfiel et al., 1995; Fig. 1). Metamorphism locally reaches amphibolite facies, but is generally low grade. The Longmenshan is intruded by a large number of plutons (Fig. 1).

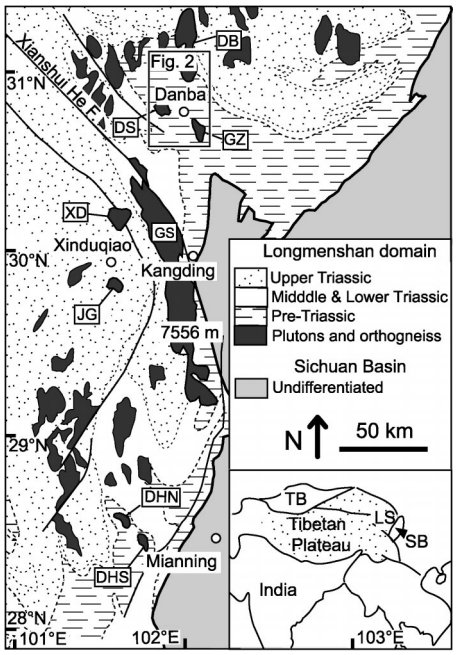

Figure 1. Simplified geological map of Longmenshan region (after Burchfiel et al., 1995). LS = Longmenshan, SB = Sichuan Basin, TB = Tarim Basin. Letters in rectangles are sample localities.

The Danba area is in the central part of Longmenshan (Fig. 1) and consists mainly of Sinian to Triassic metasediments (BGMRSP, 1991). The whole region has undergone Barrovian-type metamorphism with progressive changes from chlorite-grade slates into sillimanite-K feldspar schists (Fig. 2A) and estimated peak conditions of ~8 kbar and 700 °C (Huang et al., 2003). Deformed plutonic rocks appear at the lowest structural levels in several culminations (Fig. 2A).

The Danba region has undergone a phase of penetrative ductile deformation, D1 (Figs. 2B, C), with a NNW-SSE-oriented stretching lineation (Fig. 2B). Asymmetric pressure shadows and quartz lenses show a consistent top-to-the-S sense of shear. The alignment of metamorphic minerals shows that the D1 deformation is peak- to postpeak metamorphism

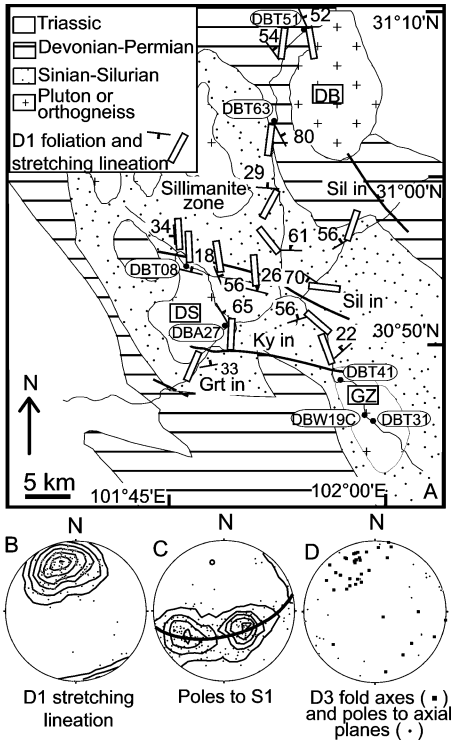

Figure 2. A: Geological map of Danba area with stratigraphic boundaries after Xu et al. (1992). Ovals give locations and numbers of samples used in dating. B: D1 stretching lineation (N = 114). C: Poles to D1 foliation (N = 211) with best-fit great circle and implied late-stage fold axis. D: D3 fold axes (N = 32) and poles to D3 axial planes (N = 37). A, B, and C are equal-area lower-hemisphere plots produced using Stereonet and contoured at 3σ levels.

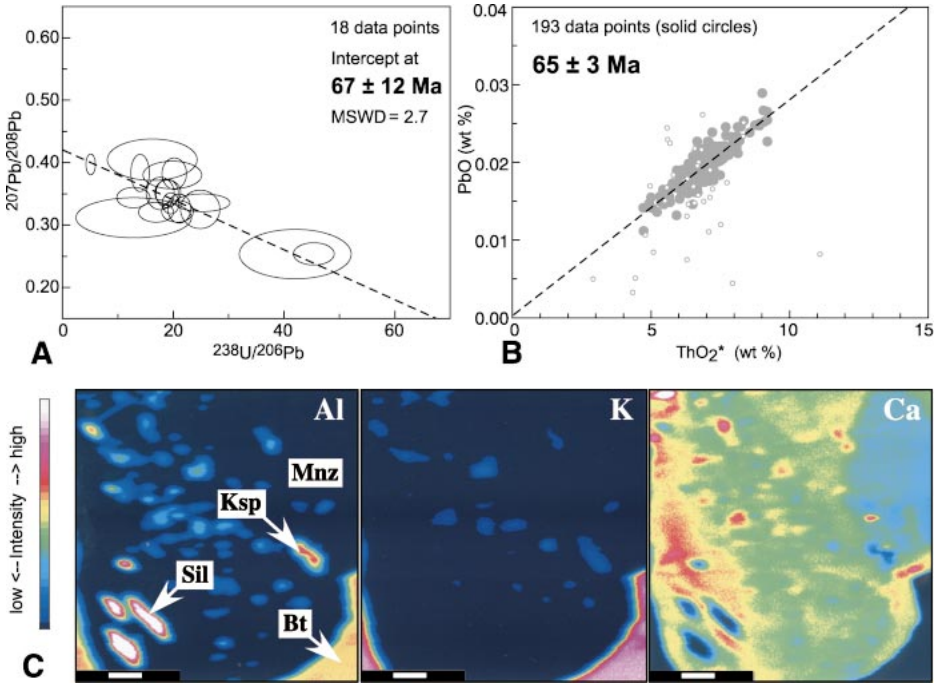

Figure 3. A: Apatite U-Pb analyses for sample DBT51. Results have been corrected for common lead by projecting along $^{204}Pb/^{206}Pb$ axis onto Terra-Wasserberg plot. B: CHIME isochron of monazite in sample DBT63. White circles are data excluded from final calculation, because analyzed spots coincided with cracks or inclusions. C: Chemical mapping of metamorphic monazite (Mnz) in DBT63 showing inclusions of sillimanite (Sil) and potassium feldspar (Ksp) and surrounding biotite (Bt). Length of white bar is 10 μm.

in age. D2 deformation is only locally developed. A stronger phase of deformation, D3, formed folds with N-S-oriented axes and steep axial planes (Fig. 2C). Locally a penetrative axial planer fabric, S3, is developed. Outcrop-scale fold profiles suggest an E-W shortening during D3 of 10%–50%, consistent with the weak development of S3.

AGE OF METAMORPHISM IN DANBA REGION

To estimate the age of metamorphism and constrain the age of ductile deformation in the Danba region, we used two methods of radiometric dating: sensitive high-resolution ion probe (SHRIMP) dating of apatite from granodiorite within the sillimanite zone (DBT51; Fig. 2A) and the chemical Th-U total lead isochron method (CHIME) dating (e.g., Suzuki and Adachi, 1991) of monazite from sillimanite-bearing pelitic schist (DBT-63). The closure temperature for U and Pb in apatite is 500–600 °C (Sano et al., 1999), somewhat less than the temperatures recorded in the adjacent schists (Huang et al., 2003). The radiometric age of this sample should, therefore, be a cooling age attained shortly after the peak of metamorphism. SHRIMP analyses of the rims of apatite grains, where reequilibration is most likely to be complete, give an age of 67 ± 12 Ma (1σ) (Fig. 3A), much younger than the previously assumed Triassic age. Monazite in the high-grade schist sample contains sillimanite aligned parallel to S1 and is contained within biotite (Fig. 3C). These microstructures clearly show that the monazite is a metamorphic mineral. The closure temperature for CHIME dating of monazite is around ~700 °C (Suzuki et al., 1994), and the age of this mineral should closely date the time during the metamorphism at which the monazite grew. The results give an age of 65 ± 3 (1σ) Ma (Fig. 3B), compatible with the apatite age and clearly showing that the peak of metamorphism in this area is Cenozoic.

STUDIED PLUTONS AND RELATIONSHIP TO DEFORMATION

The discovery of Cenozoic regional metamorphism in the central Longmenshan contradicts the generally held view that the tectonic metamorphism in this region is Mesozoic and unrelated to the formation of the Tibetan Plateau. How widespread is this event? The primary constraint on the age of regional deformation and metamorphism in the Longmenshan comes from radiometric ages of posttectonic plutons. There are two major sources of uncertainty in these estimates. First, some of the plutons show moderate to strong deformation. In particular, our field studies have shown that the plutons of the Danba area are strongly deformed (Fig. 4A) and their formation ages give an older limit on deformation, not a younger limit. Second, nearly all the available age data are biotite K-Ar ages, which should give cooling ages and not intrusion ages. The ages show a large scatter from pre-Triassic to Cenozoic (Fig. 5). There has been no attempt to assess the significance of this variation.

To address these problems, we sampled eight granitic plutons from between 28° and 31°N for zircon U-Pb, mica $^{40}Ar/^{39}Ar$ dating, and structural studies. We define four distinct areas (Fig. 1).

Dahebian Area

The Dahebian area consists mainly of slates and schists locally with amphibolite-grade mineral assemblages intruded by two plutons referred to as Dahebian south (DHS) and Dahebian north (DHN). The main deformation produces a flat-lying schistosity with an E-W-oriented stretching lineation. Subsequent deformation produced a series of upright folds and a locally well-developed cleavage. Both DHN and DHS intrude across the main schistosity. DHS is affected by the upright folding (Fig. 4D).

Xinduqiao Area

In the Xinduqiao area two granodiorite plutons, Xinduqiao and Jaggai, apparently intrude across the axes of regionally developed upright folds and associated faults (Burchfiel et al.,1995). The microstructure of cordierite por-

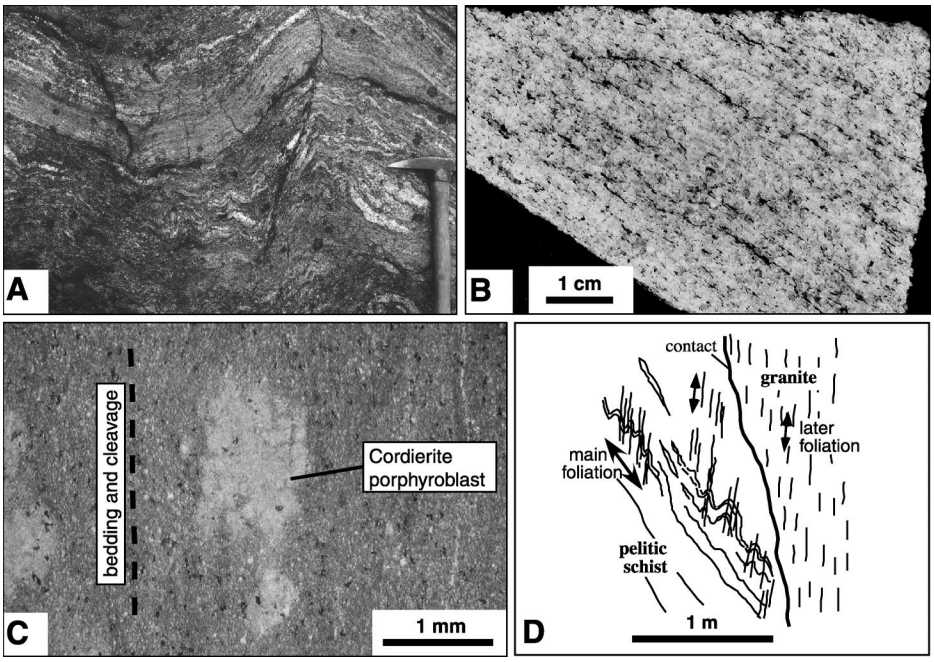

Figure 4. A: Strongly deformed granite sample from Danba area. B: D3 folds deforming S1 in Danba area. C: Photomicrograph of slate from contact-metamorphic aureole around JG pluton (plane polarized light). Vertical bedding and cleavage are overgrown by cordierite porphyroblast showing that intrusion of pluton is postkinematic. D: Field sketch of contact between Dahebian south granite and surrounding schists. Intrusion postdates main deformation, but is overprinted by later upright folding.

phryoblasts formed in the contact-metamorphic aureole around the plutons confirms the postkinematic nature of the intrusions (Fig. 4C). However, cryptic postgrowth deformation was also locally observed.

Gongashan Area

The Gongashan area consists of a large pluton that locally has a subvertical foliation related to movement on the major Xianshui He strike-slip fault (Roger et al., 1995).

Danba Area

The three plutons studied in the Danba area are Gezhong, Dasan, and Danba. All three are locally strongly deformed (Fig. 4A).

FORMATION AND COOLING AGES OF PLUTONS

Dating Methods

In this study we combine zircon U-Pb dating with muscovite and biotite $^{40}Ar/^{39}Ar$ dating. These three methods have contrasting closure temperatures, and the age data can be used to discuss the thermal history of the plutons. Our results can also help verify the geological significance of the ages by observing if they form a predictable sequence corresponding to the order of their closure temperatures. With the exception of the Danba area and one age from the JG pluton, the ages from the three methods are in a sequence compatible with their accepted closure temperatures (Hames and Bowring, 1994; Grove and Harrison, 1996; Cherniak and Watson, 2000).

Because the closure temperature for U-Pb dating of zircon is high, these ages are interpreted as formation ages of the plutons (Table 1). We used cathodoluminescence images to help distinguish inherited cores from in situ growth and mainly measured rims of large idiomorphic grains. All the results plot on concordia and the rim data are consistent at the 1σ level. We carried out $^{40}Ar/^{39}Ar$ dating of single grains of biotite and muscovite with step heating to estimate cooling ages of the plutons (Table 1). Where plateau ages cannot be defined, ages are given as weighted means of consistent steps (Ludwig, 2001). More details of the dating results are available as archive material[1].

Results and Interpretation of Pluton Age Data

The Dahebian plutons formed ca. 176 Ma and cooled slowly (Table 1), reaching the closure temperature for Ar in biotite 60–70 m.y. after intrusion (Fig. 5A). The slow cooling rate suggests that the pluton intruded into relatively high temperature rocks, and this is consistent with the local presence of amphibolite-grade rocks.

In the Xinduqiao area plutons formed ca. 196 Ma. Two biotite $^{40}Ar/^{39}Ar$ ages are ca. 195 Ma. Other biotite samples showing some signs of subsolidus alteration yielded similar but slightly scattered ages. These results suggest that the plutons cooled to the closure temperature for Ar in biotite within a few million years of intrusion (Table 1; Fig. 5B). Rapid initial cooling is consistent with the low grade of the surrounding Triassic sediments.

In both the Dahebian and Xinduqiao areas pluton intrusion clearly postdates the main tectonic fabrics, showing that the age of regional deformation in these areas is Triassic. The differences in cooling rates revealed here probably reflect differences in the depth of intrusion and may be the principal cause of the wide spread of biotite K-Ar ages (Fig. 5B).

Our new $^{40}Ar/^{39}Ar$ muscovite plateau age of 5.5 Ma (Fig. 5A) from the Gongashan pluton is consistent with the estimated 12 Ma formation age (Roger et al., 1995).

The Gezhong pluton in the Danba area has a U-Pb zircon age of 771 Ma (Table 1), suggesting that this is part of the Yangtze craton (e.g., Roger and Calassou, 1997). The $^{40}Ar/^{39}Ar$ mica ages range from 102 Ma to 48 Ma (Table 1) with a clear cluster around 50 Ma.

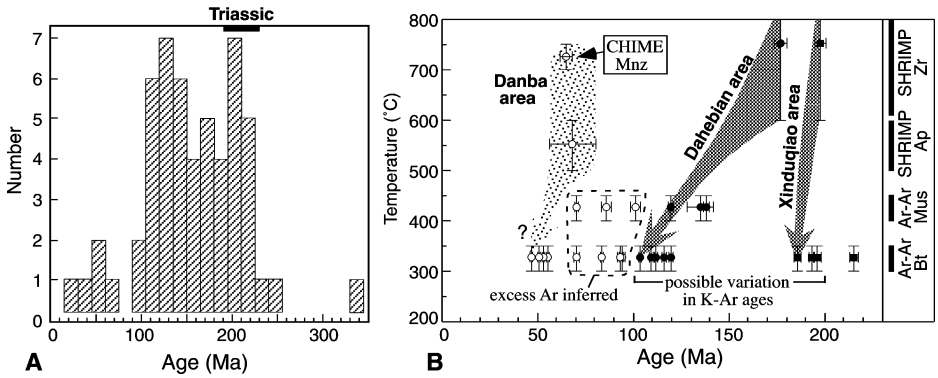

Figure 5. A: Results of K-Ar dating of plutons (Burchfield et al., 1995) between 28° and 31°N in Longmenshan sorted in 15 m.y. bins. B: Shaded areas show cooling histories for Dahebian, Xinduqiao, and Danba areas based on radiometric dating and corresponding closure temperatures (errors are 1σ or 66% confidence limits).

[1]GSA Data Repository item 2003119, Table DR1, sample locations, and Figures DR1 and DR2, details of dating, is available online at www.geosociety.org/pubs/ft2003.htm, or on request from editing@geosociety.org or Documents Secretary, GSA, P.O. Box 9140, Boulder, CO 80301–9140, USA.

TABLE 1. SUMMARY OF RADIOMETRIC DATING OF PLUTONS

Region	Pluton	Sample	Shrimp U-Pb			$^{40}Ar/^{39}Ar$ (Mus)			$^{40}Ar/^{39}Ar$ (Bt)		
			Min.	Age (rim)	MSWD	Type	Age	MSWD	Type	Age	MSWD
Danba	DB (gd)	DBT51	Ap	67 ± 24	2.7				wm	52.2 ± 0.6	8.3
	DS (gr)	DBA27							wm	54.6 ± 0.9	3.9
	DS (gr)	DBT08							pl (76.7)	70.9 ± 2.4	1.6
	GZ (gr)	DBT31				wm	102.2 ± 2.4	14	pl (72.7)	55.1 ± 1.2	1.3
	GZ (gr)	DBT31				wm	86.5 ± 2.4	29	pl (60.3)	47.7 ± 1.2	1.5
	GZ (gr)	DBT41	Zr	771 ± 39	0.21				wm	84.7 ± 0.9	3.4
	GZ (apl)	DBW19c							wm	94.1 ± 2.1	9.3
	GZ (apl)	DBW19c				pl (74.8)	70.9 ± 1.2	0.7	pl (73.2)	94.3 ± 1.6	0.81
Xinduqiao	XD (gd)	XDT-01	Zr	196 ± 7	0.18				wm	186.6 ± 1.7	5.1
	JG (gd)	JGT-01							wm	216.1 ± 2.3	3.7
	JG (gd)	JGT-01							pl (70.1)	194.3 ± 2.4	0.89
	JG (gd)	JGT-02							wm	194.6 ± 1.6	3.7
	JG (gd)	JGT-02							wm	196.6 ± 2.8	8
Dahebian	DHS (gr)	DHT-04							pl (93.4)	110.3 ± 1.0	1.5
	DHS (gr)	DHT-04							pl (93.3)	120.5 ± 1.9	1.18
	DHS (gr)	DHT-05	Zr	176 ± 7	0.42	wm	136 ± 7	9.4	pl (83.3)	104.3 ± 1.4	1
	DHS (gr)	DHT-09				wm	139.1 ± 1.5	1.8			
	DHS (gr)	DHT-09				pl (78.1)	120.6 ± 1.4	1.5			
	DHN (gr)	DHT-03							pl (92.1)	116.6 ± 1.0	0.87
	DHN (gr)	DHT-03				pl (84.6)	120.4 ± 1.8	0.81	pl (84.2)	112.7 ± 1.2	1.7
Gonga	GS (gr)	EDT-02				pl (80.1)	5.5 ± 0.2	1.5			

Note: The errors are given as 2σ or 95% confidence limits. $^{40}Ar/^{39}Ar$ ages are given as either plateau ages (pl) or weighted mean ages (wm). The percentage of ^{39}Ar used to define the plateau is given in brackets. The SHRIMP (II) U-Pb and $^{40}Ar/^{39}Ar$ dating was carried out at Hiroshima University and Okayama University of Science, respectively. Zircon SHRIMP ages and errors are calculated from weighted means of $^{238}U/^{206}Pb$ ages and errors. Mus—muscovite, Bt—biotite, Ap—apatite, Zr—zircon, MSWD—mean square of weighted deviates, DHS—Dahebian south, DHN—Dahebian north, XD—Xinduqiao, JG—Jaggai, GS—Gongashan, DB—Danba, DS—Dasan, GZ—Gezhong, gd—granodiorite, gr—granite, apl—aplite.

It is significant that all of the $^{40}Ar/^{39}Ar$ ages are younger than any of the results from either the Dahebian or Xinduqiao areas (Fig. 5B). The ages are too diverse over too small an area to be explained as the result of local differences in cooling rates; we propose that the spread in ages is due to incomplete degassing during the ca. 65 Ma Danba metamorphism, the cluster of ages around 50 Ma representing a cooling age (Fig. 5B). Biotite ages older than muscovite ages in sample DBW19C support this interpretation.

IMPLICATIONS FOR TECTONICS OF EASTERN TIBET

Our work has confirmed the conclusion of earlier studies that most of the upper crustal deformation in the Longmenshan orogen is Mesozoic. However, we have also revealed the presence of a ca. 65 Ma Barrovian metamorphism and related deformation in the Danba area. These results give an important test of models that suggest that thickening in the eastern margin of Tibet took place by solid-state midcrustal flow.

The Danba metamorphic rocks represent a zone of ductile flow overlain by low-grade rocks deformed nearly exclusively in the Mesozoic and underlain by basement rocks of the Yangtze craton. Both the type and structural position of these metamorphic rocks are consistent with the idea of solid-state intrusion of mid-crustal material. However, deformation in the Danba area is associated with a N–S stretching direction, roughly perpendicular to the line of maximum topographic gradient and not parallel. This implies that the Cenozoic ductile deformation was not driven by gradients in the Tibetan surface topography. We cannot exclude the possibility of rotation of the lineations since their formation, but the presence of consistent Mesozoic fold and foliation trends suggests that such rotation is limited. A second important point is the age of metamorphism and deformation. The presence of high-grade Barrovian metamorphism ca. 65 Ma implies that the crust was already thick before the onset of India-Asia collision (ca. 54 Ma). D3 in the Danba region represents a significant phase of 10%–50% E-W shortening younger than 65 Ma, and we conclude that the D3 deformation is sufficient to explain most, if not all, the development of the present crustal thickness.

Midcrustal flow is a likely cause of the flat topography of Tibet. However, there is no need to invoke this process to account for either the surface geology or crustal thickness of the Longmenshan; we suggest that this process occurs on shorter length scales than those previously proposed.

ACKNOWLEDGMENTS

We thank Z. Chen and L. Zheng for their help in the field. We also thank Y. Tsutsumi for advice on U-Pb dating, T. Niwa for assistance with the chemical mapping, and C. Gozu for assistance with the $^{40}Ar/^{39}Ar$ dating. E. Kirby and L. Ratschbacher gave useful and constructive reviews.

REFERENCES CITED

Burchfiel, B.C., Zhiliang, C., Yuping, L., and Royden, L.H., 1995, Tectonics of the Longmen Shan and adjacent regions, central China: International Geology Review, v. 37, p. 661–735.

Bureau of Geology and Mineral Resources of Sichuan Province, 1991, Regional geology of Sichuan Province: Beijing, Geological Publishing House, 730 p. (in Chinese with English summary).

Cherniak, D.J., and Watson, E.B., 2000, Pb diffusion in zircon: Chemical Geology, v. 172, p. 5–24.

Clark, M.K., and Royden, L.H., 2000, Topographic ooze: Building the eastern margin of Tibet by lower crustal flow: Geology, v. 28, p. 703–706.

Dirks, P.H.G.M., Wilson, C.J.L., Chen, S., Luo, Z.L., and Liu, S., 1994, Tectonic evolution of the NE margin of the Tibetan Plateau; evidence from the central Longmen Mountains, Sichuan Province, China: Journal of Southeast Asian Earth Sciences, v. 9, p. 181–192.

Fielding, E., Isacks, B., Barazangi, M., and Duncan, C.C., 1994, How flat is Tibet?: Geology, v. 22, p. 163–167.

Grove, M., and Harrison, T.M., 1996, ^{40}Ar diffusion in Fe-rich biotite: American Mineralogist, v. 81, p. 940–951.

Hames, W.E., and Bowring, S.A., 1994, An empirical evaluation of the argon diffusion geometry in muscovite: Earth and Planetary Science Letters, v. 124, p. 161–167.

Holt, W.E., and Wallace, T.C., 1990, Crustal thickness and upper mantle velocities in the Tibetan plateau region from the inversion of regional Pnl waveforms: Evidence for a thick upper mantle lid beneath southern Tibet: Journal of Geophysical Research, v. 95, no. B8, p. 12,499–12,525.

Hou, J., Uemura, T., Xueming, L., and Toyoshima, T., 1995, Meso- and micro-structures and their tectonic implications in the middle segment of the Longmenshan Nappe structure zone, Sichuan Province, southwest China: Geological Society of Japan Journal, v. 101, p. 315–332.

Huang, M.-H., Buick, I.S., and Hou, W., 2003, Tectonometamorphic evolution of the eastern Tibet plateau: Evidence from the central Songpan-Garze orogenic belt, western China: Journal of Petrology, v. 44, p. 255–278.

Kirby, E., Reiners, P.W., Krol, M.A., Whipple, K.X., Hodges, K.V., and Farley, K.A., 2002, Late cenozoic evolution of the eastern margin of the Tibetan plateau: Inferences from $^{40}Ar/^{39}Ar$ and U-Th/He thermochronology: Tectonics, v. 21, p. 1–20.

Ludwig, K.R., 2001, Users manual for Isoplot 2.49: Berkeley Geochronology Center Special Publication 1a, 58 p.

Roger, F., and Calassou, S., 1997, Géochronologie U-Pb sur zircons et géochimie (Pb, Sr et Nd) du socle de la chaîne de Songpan-Garze (Chine): Paris, Académie des Sciences Comptes Rendus, Ser. IIa, v. 324, p. 819–826 (in French with English summary).

Roger, F., Calassou, S., Lancelot, J., Malavielle, J., Mattauer, M., Zhiqin, X., Ziwen, H., and Liwei, H., 1995, Miocene emplacement and deformation of the Konga Shan granite (Xianshui He fault zone, west Sichuan, China): Geodynamic implications: Earth and Planetary Science Letters, v. 130, p. 201–216.

Rowley, D.B., 1996, Age of initiation of collision between India and Asia: Overview of stratigraphic data: Earth and Planetary Science Letters, v. 145, p. 1–13.

Royden, L.H., Burchfiel, B.C., King, R.W., Wang, E., Chen, Z., Shen, F., and Liu, Y., 1997, Surface deformation and lower crustal flow in eastern Tibet: Science, v. 276, p. 788–790.

Sano, Y., Oyama, T., Terada, K., and Hidaka, H., 1999, Ion microprobe U-Pb dating of apatite: Chemical Geology, v. 153, p. 249–258.

Suzuki, K., and Adachi, M., 1991, Precambrian provenance and Silurian metamorphism of the Tsubonosawa paragneiss in the South Kitakami terrane, northeast Japan, revealed by the chemical Th-U-total Pb isochron ages of monazite, zircon and xenotime: Geochemical Journal, v. 25, p. 357–376.

Suzuki, K., Adachi, M., and Kajizuka, I., 1994, Electron microprobe observations of Pb diffusion in metamorphosed detrital monazites: Earth and Planetary Science Letters, v. 128, p. 391–405.

Xu, Z.Q., Hou, L.W., Wang, Z.X., Fu, X.F., and Huang, M.H., 1992, Orogenic processes of the Songpan—Garze orogenic belt of China: Beijing, Geological Publishing House, 909 p. (in Chinese).

Manuscript received 1 February 2003
Revised manuscript received 27 May 2003
Manuscript accepted 29 May 2003

Printed in USA

DR2003119

Captions for Supplementary Material

Fig. 1. 40Ar/39Ar heating spectra for the pluton samples in the Dahebian, Xinduqiao, and Gohgashan areas (Fig. 1a) and the Danba area (Fig. 1b).

Fig. 2. Tera-Wasserberg plots for all analyzed zircon spots including both core and rim with 2σ error ellipses. 2a. Sample DHT-05, The isolated results of approximately 500 Ma, 900 Ma and 2,400 Ma all represent core analyses. 2b. Sample DBT-41. If the relatively young age given by the r7 analysis is excluded from the calculation the result becomes 814 ± 43 Ma. 2c. Sample XDT-01. The isolated result of approximately 400 Ma comes from a core analysis.

Table 1.
Zircon SHRIMP data.

Table 2.
Apatite SHRIMP data

Table 3.
Location of samples used for dating in this study.

Fig. 1a

DAHEBIAN REGION

S Pluton

DHT 03 (bt) 1

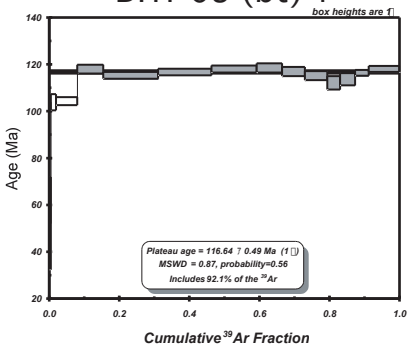

DHT 03 (bt) 2

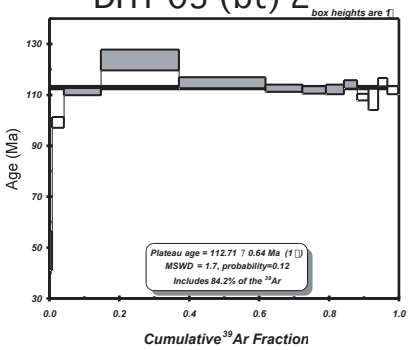

DHT 03 (ms)

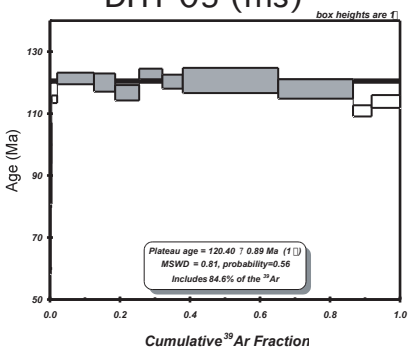

N Pluton

DHT 04 (bi) 1

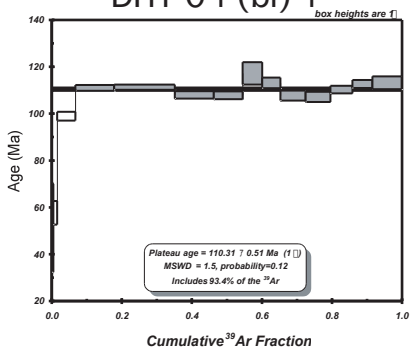

DHT 04 (bi) 2

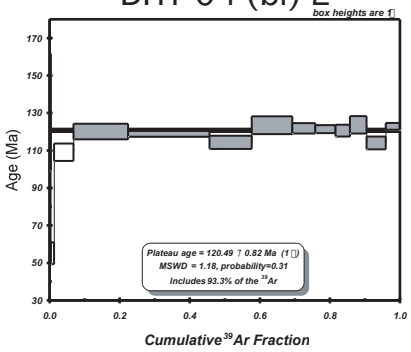

DHT 05 (bi)

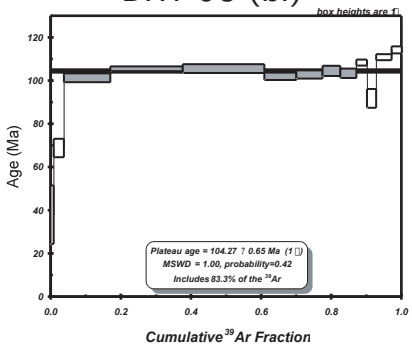

DHT 05 (ms)

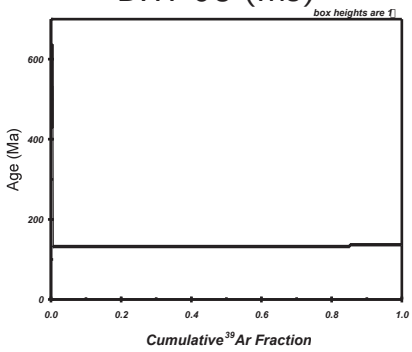

DHT 09 (ms) 1

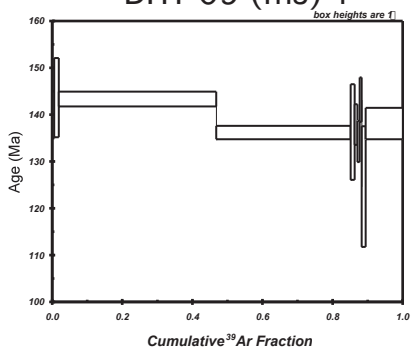

DHT 09 (ms) 2

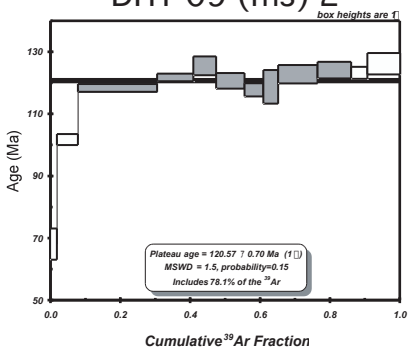

XINDUQIAO and GONGASHAN REGIONS

JGT 01 (bt) 1

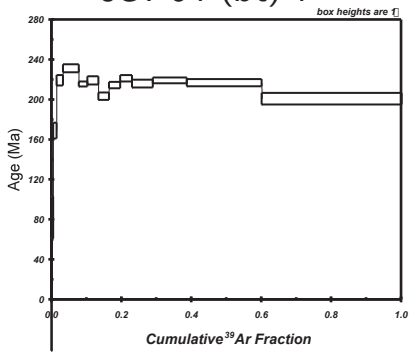

JGT 01 (bt) 2

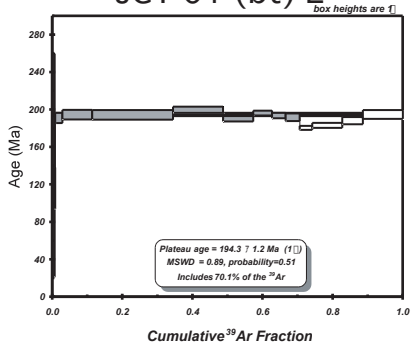

JGT 02 (bt) 1

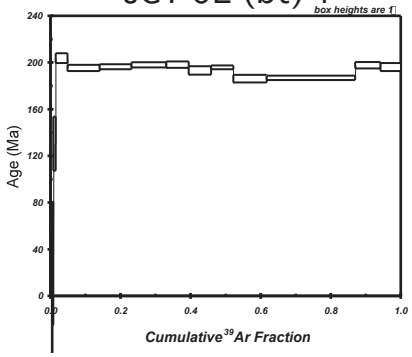

JGT 02 (bt) 2

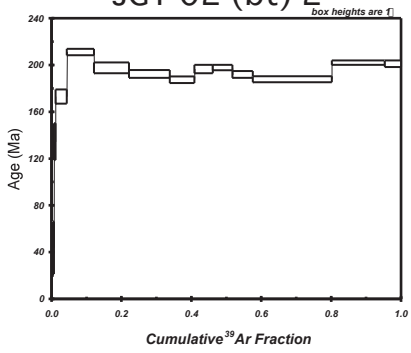

XDT 01 (bt)

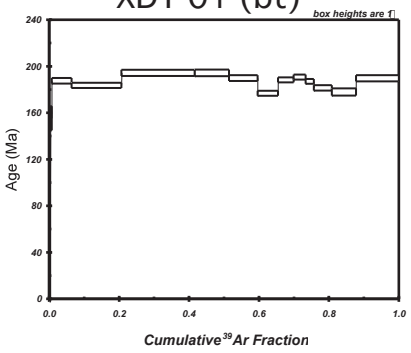

EDT 02 (ms)

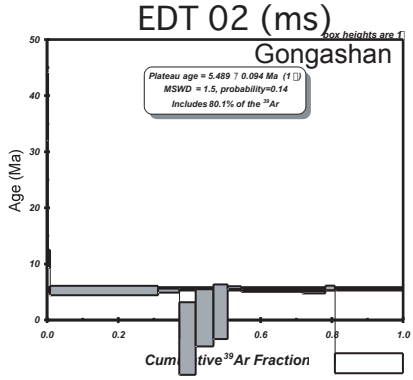

Fig. 1b

DANBA REGION

DBW 19c(bt) 1

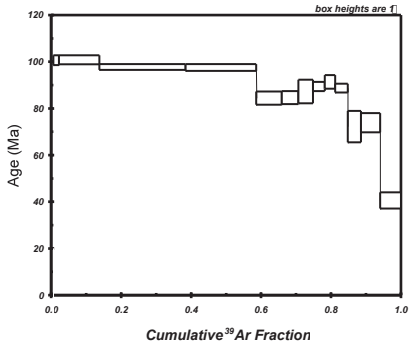

DBW 19c(bt) 2

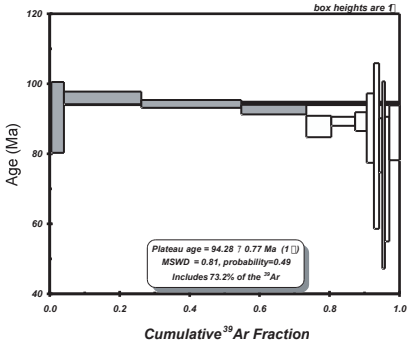

DBW 19c(ms)

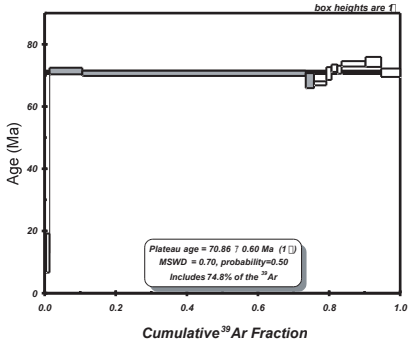

Gezhong

DBT 31(bt) 1

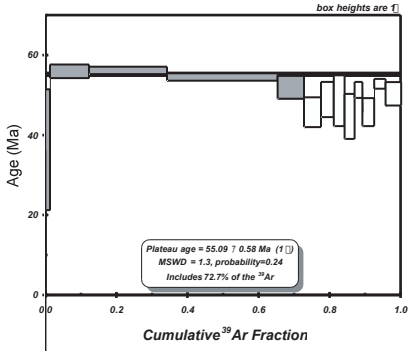

DBT 31(bt) 2

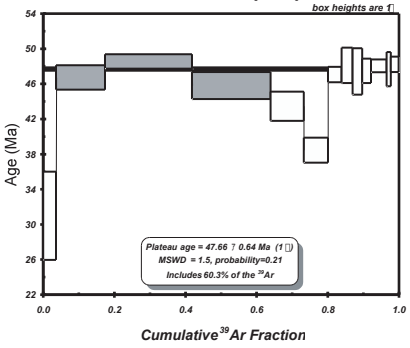

DBT 31(ms) 1

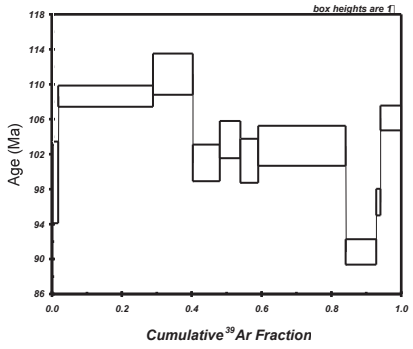

DBT 31(ms) 2

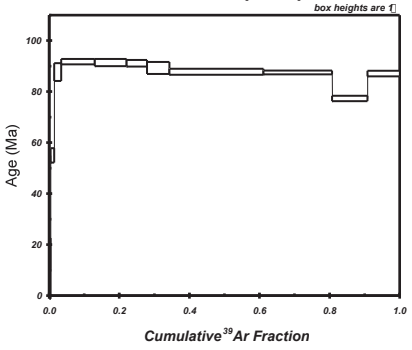

DBT 41(bt)

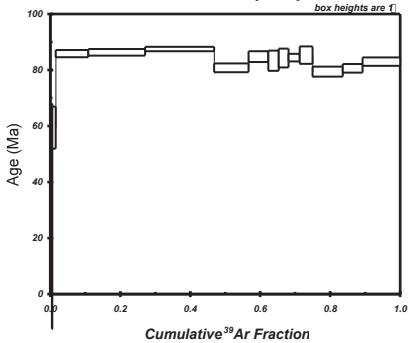

Dasan

DBA 27(bt)

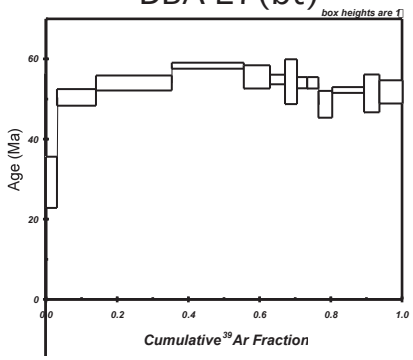

DBT 08(bt)

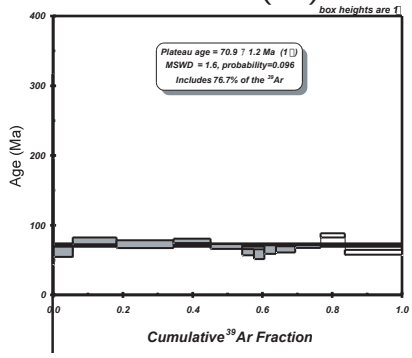

N Pluton

DBT 51(bt)

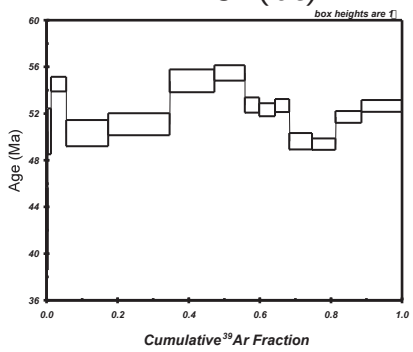

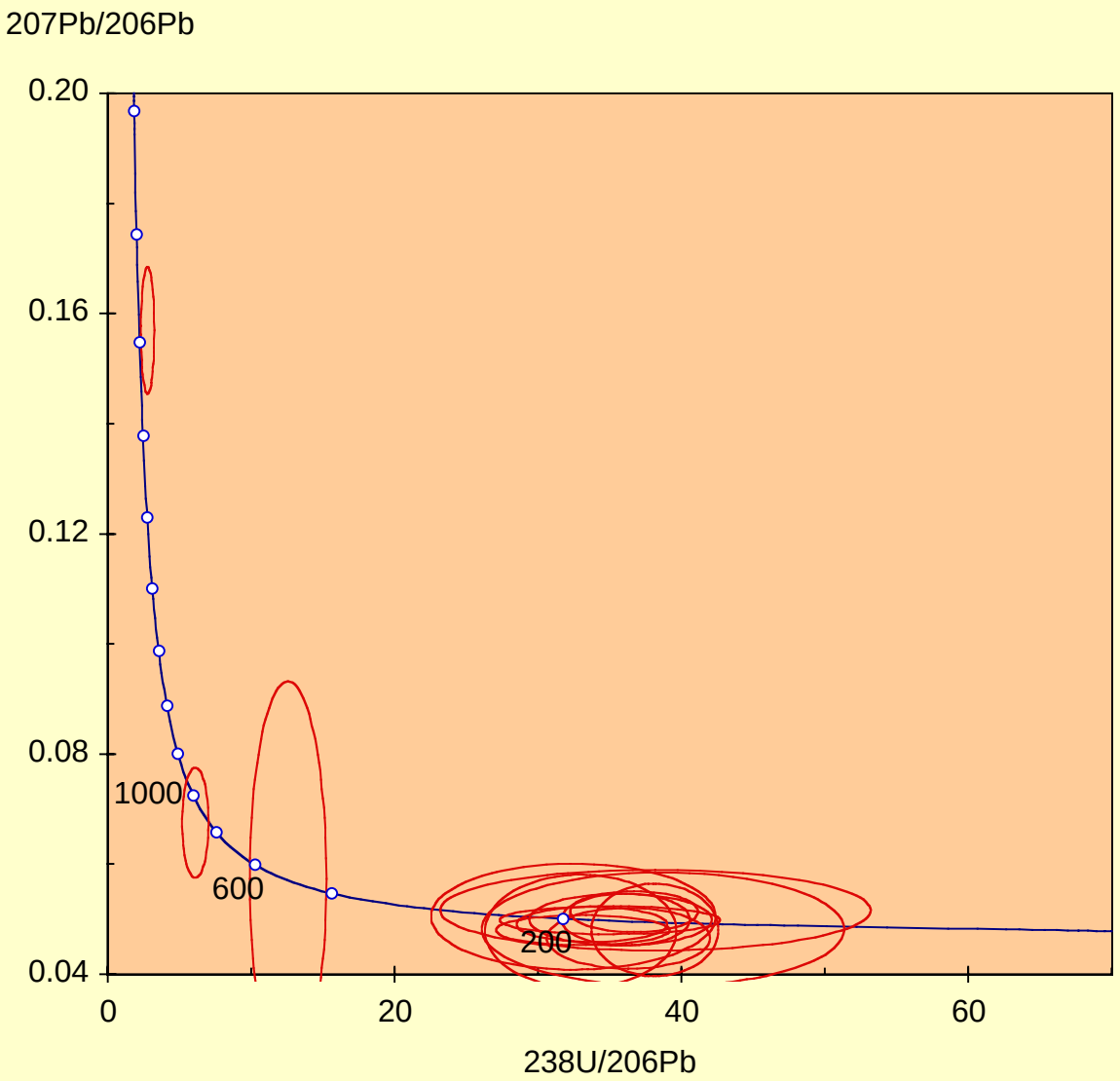
207Pb/206Pb
0.20
0.16
0.12
0.08
0.04
1000
600
200
0
20
40
60
238U/206Pb

Fig. 2a

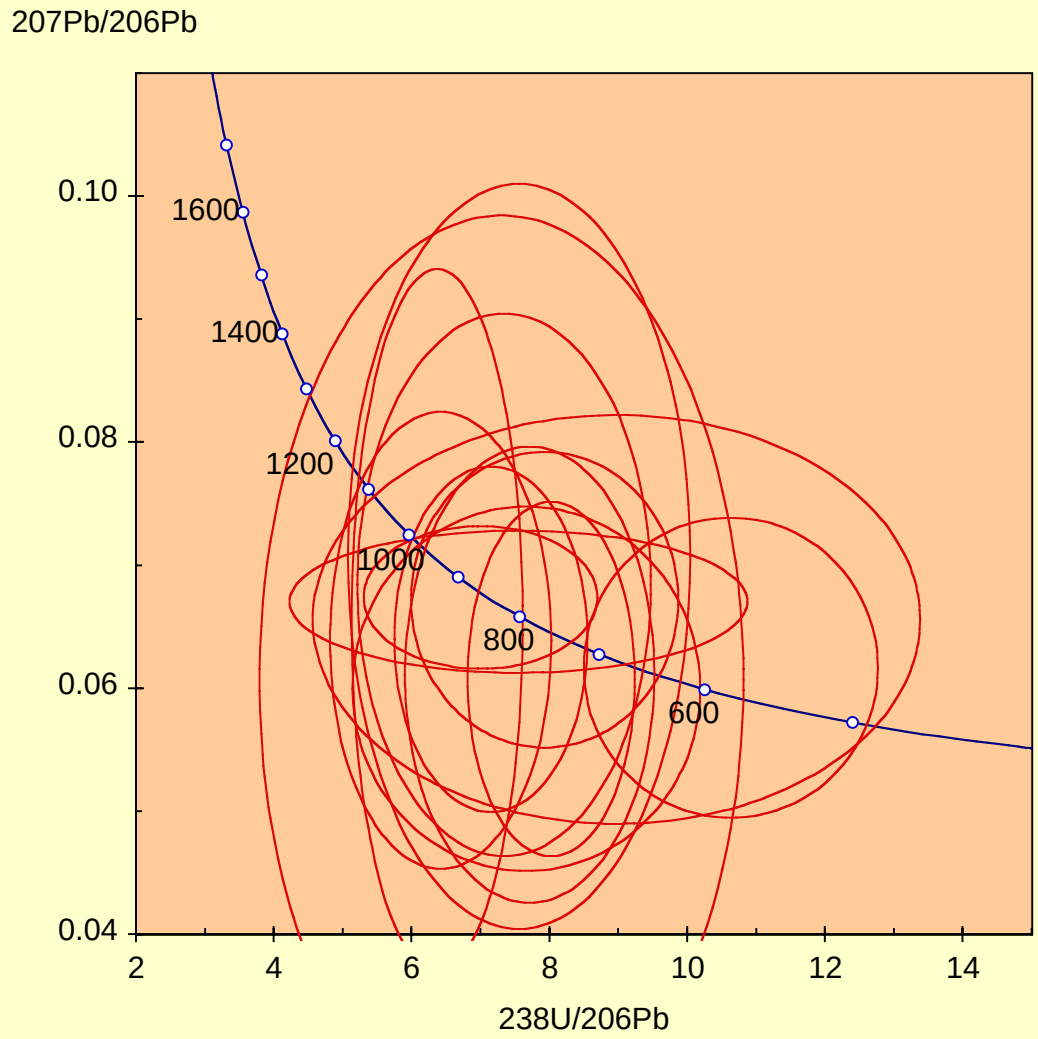
207Pb/206Pb
0.10
0.08
0.06
0.04
1600
1400
1200
1000
800
600
2
4
6
8
10
12
14
238U/206Pb

Fig. 2b

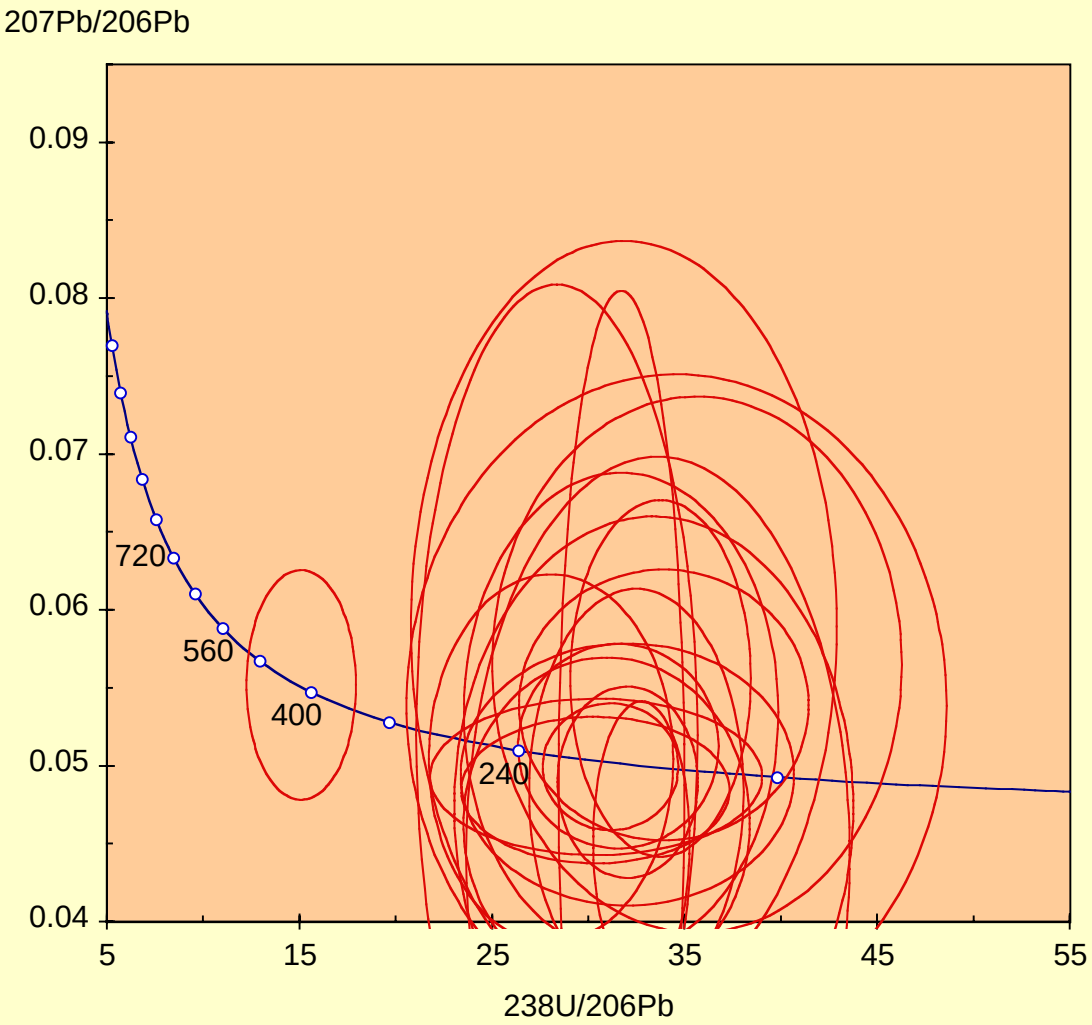
207Pb/206Pb
0.09
0.08
0.07
0.06
0.05
0.04
720
560
400
240
5
15
25
35
45
55
238U/206Pb

Fig. 2c

Zircon SHRIMP analyses

Labels	$^{204}Pb/^{206}Pb$	err	$^{207}Pb/^{206}Pb$	err	$^{208}Pb/^{206}Pb$	err	F-value	err	$^{238}U/^{206}Pb^*$	err	$^{207}Pb^*/^{206}Pb^*$	err	^{238}U-^{206}Pb age	err	^{207}Pb-^{206}Pb Ag	err	U ppm	
DBT41-c1	0.00148	0.00066577	0.082113	0.010591	0.15118	0.023148	0.025703	0.011562	7.3063	1.4349	0.060675	0.015423	826.92	152.41	627.75	469.92	54.625	
DBT41-c2	0.00087916	0.00033928	0.076562	0.0052019	0.14504	0.013061	0.015107	0.0058302	6.4229	0.65628	0.063881	0.0075877	932.8	88.736	737.7	233.16	103.53	
DBT41-c3	0.0025112	0.00051246	0.10443	0.0020076	0.19433	0.0056695	0.043629	0.0089034	7.3447	0.86925	0.068394	0.0090085	822.87	91.428	880.5	251.06	62.575	
DBT41-c4	0.0020607	0.00066741	0.095162	0.0032132	0.16867	0.0074515	0.03539	0.011462	6.3729	0.50681	0.065498	0.011675	939.61	69.533	790.38	335.29	39.765	
DBT41-r1	0.00066625	0.00020854	0.07676	0.0035665	0.1332	0.01836	0.011641	0.0036436	7.932	0.79212	0.067183	0.004911	765.41	72.074	843.46	145.14	127.63	
DBT41-r10	0.00047467	9.97E-05	0.074194	0.0017515	0.13768	0.0033184	0.0082159	0.001726	6.9995	0.69286	0.067374	0.0023696	860.86	79.77	849.36	71.459	127.26	
DBT41-r2	0.0012631	0.00036293	0.078261	0.0012317	0.11825	0.013213	0.022016	0.0063256	7.6653	1.0309	0.059947	0.0060525	790.48	100.05	601.65	204.7	81.756	
DBT41-r3	0.002624	0.00051441	0.10825	0.0082653	0.18659	0.02047	0.045689	0.0089568	7.5612	1.0157	0.070701	0.012374	800.71	101.15	948.77	322.2	135.22	
DBT41-r4	0.00059261	0.00010987	0.075542	0.0015653	0.12437	0.0068463	0.010318	0.0019128	7.5522	1.3583	0.067023	0.0023585	801.61	135.57	838.5	71.614	81.766	
DBT41-r5	0.0012227	0.00035882	0.083201	0.0033593	0.13251	0.011109	0.021538	0.0063205	8.975	1.8008	0.065587	0.0067886	680.99	129.67	793.24	203.3	113.33	
DBT41-r6	0.00032513	9.82E-05	0.068664	0.005496	0.14029	0.0083057	0.0056372	0.001702	7.1517	0.57271	0.063973	0.0057395	843.68	63.328	740.73	179.16	77.954	
DBT41-r7	0.0010039	0.00019883	0.076187	0.0037379	0.088566	0.0051475	0.017853	0.0035361	10.635	0.87189	0.061654	0.0049864	579.34	45.426	662.14	164.42	196.25	
DBT41-r8	0.0017457	0.00029912	0.086029	0.003051	0.12643	0.006944	0.030526	0.0052307	8.0282	0.4955	0.060739	0.005883	756.76	44.069	630.01	195.97	61.768	
DBT41-r9	0.0020291	0.00040566	0.090473	0.0031994	0.15157	0.0057823	0.035383	0.0070738	7.7143	0.73899	0.061092	0.0075744	785.75	70.864	642.46	246.26	76.373	
DHT05-c1	0.00053042	0.00015262	0.075133	0.0032721	0.16294	0.0070292	0.0090729	0.0026107	6.1058	0.37425	0.067517	0.0040935	977.75	55.608	853.77	121.13	211.02	
DHT05-c2	0.00019802	2.94E-05	0.053368	0.0038884	0.81124	0.065477	0.0036435	0.00054185	32.462	4.0515	0.050461	0.0039301	195.59	24.045	216.27	171	4984.5	
DHT05-c3	0.0041693	0.00075688	0.11804	0.0043042	0.24729	0.014135	0.074737	0.013568	12.582	1.0882	0.05736	0.014644	493.01	41.051	505.39	480.65	40.549	
DHT05-c4	4.60E-05	7.23E-06	0.15753	0.0046909	0.0093173	0.00065999	0.00069925	0.00010982	2.7788	0.18935	0.15694	0.0046955	1981.5	116.24	2422.9	49.885	1278.2	
DHT05-r1	0.00028242	7.65E-05	0.053185	0.00045052	0.097335	0.0016286	0.0051997	0.0014083	33.764	2.1469	0.04903	0.0012911	188.16	11.791	149.27	60.584	1502.2	
DHT05-r10	0.00047813	0.00010998	0.056939	0.00076446	0.060854	0.0022647	0.0088106	0.0020265	35.765	2.6021	0.049913	0.001914	177.77	12.757	190.96	86.838	802.93	
DHT05-r11	0.00027606	7.30E-05	0.055671	0.0027399	0.12296	0.011744	0.0050919	0.0013466	38.179	6.1359	0.051623	0.002986	166.67	26.444	268.75	127.51	1726.8	
DHT05-r2	0.00025117	4.69E-05	0.053495	0.0007186	0.092385	0.0018794	0.0046268	0.00086427	35.007	3.1431	0.049803	0.0010344	181.56	16.074	185.82	47.655	1797	
DHT05-r3	0.00016577	4.85E-05	0.050431	0.00080738	0.084373	0.0028015	0.0030512	0.00089195	33.128	2.4676	0.04799	0.0011124	191.71	14.069	98.752	53.951	1776.8	
DHT05-r4	0.00049757	0.00019958	0.055155	0.0026978	0.055077	0.0042259	0.0091575	0.003673	32.979	2.723	0.047824	0.0041866	192.56	15.664	90.594	195.3	1088.8	
DHT05-r5	0.00050649	0.0002087	0.055652	0.0025584	0.080231	0.0031418	0.0093437	0.0038501	38.719	5.1638	0.048194	0.0042122	164.38	21.645	108.78	194.37	1045.7	
DHT05-r6	0.00016134	5.43E-05	0.053731	0.0012466	0.33438	0.0088244	0.0029742	0.0010003	36.697	1.8212	0.051365	0.0015142	173.31	8.4865	257.24	66.374	1300.6	
DHT05-r7	0.00054709	0.00012176	0.054589	0.0011112	0.064412	0.0031722	0.010084	0.0022443	36.31	2.3242	0.046516	0.0022449	175.14	11.06	24.445	111.9	881.7	
DHT05-r8	0.00073975	0.00019211	0.058938	0.0014455	0.058298	0.0021921	0.013644	0.0035433	38.15	1.8113	0.048043	0.0034205	166.8	7.8176	101.37	160.26	656.79	
DHT05-r9	0.00039644	0.00011149	0.055767	0.00071269	0.079752	0.0017789	0.0073064	0.0020547	36.112	1.8302	0.049942	0.0019103	176.09	8.8034	192.29	86.606	1372.2	
XDT01-c1	0.0025636	0.00071436	0.08646	0.0037836	0.23388	0.010036	0.047151	0.013139	31.719	1.334	0.048735	0.012965	200.1	8.2865	135.09	528.61	117.99	
XDT01-c2	0.0015309	0.00032853	0.081172	0.0082727	0.22297	0.01992	0.028158	0.0060428	31.846	4.5171	0.058931	0.01011	199.31	27.838	564.55	335.41	236.14	
XDT01-c3	0.00032966	8.88E-05	0.053289	0.0012972	0.020764	0.0014495	0.0060589	0.0016317	30.375	2.8463	0.048436	0.0019182	208.81	19.253	120.63	90.755	1278.5	
XDT01-c4	0.00015297	4.03E-05	0.057418	0.0029361	0.0885	0.0043608	0.0027617	0.00072737	15.091	1.1597	0.055185	0.0030115	413.61	30.786	419.73	117.44	964.71	
XDT01-c5	0.0010096	0.00026658	0.065278	0.002089	0.2496	0.0077936	0.018529	0.0048924	28.068	2.5911	0.050452	0.0048267	225.67	20.473	215.87	207.64	272.79	
XDT01-c6	0.0023837	0.00061433	0.086888	0.0051212	0.30019	0.019567	0.043755	0.011277	28.371	2.982	0.051952	0.01182	223.31	23.069	283.31	450.79	117.07	
XDT01-r1	0.00091492	0.00021366	0.058618	0.001276	0.13023	0.0028275	0.016837	0.0039318	32.755	1.0232	0.045093	0.0036944	193.86	5.9659	0.00074635	137.62	686.81	
XDT01-r10	0.00086125	0.00027264	0.060987	0.0029532	0.11277	0.0068312	0.015847	0.0050166	32.496	2.2741	0.048307	0.0053306	195.38	13.468	114.31	241.54	815.77	
XDT01-r11	0.00077709	0.00025173	0.065199	0.0075825	0.14803	0.019063	0.014312	0.0046364	34.584	5.7311	0.053837	0.0086969	183.75	30.021	364.22	328.18	434.16	
XDT01-r12	0.0018881	0.00042732	0.075153	0.0024588	0.16982	0.0066024	0.034757	0.0078661	33.398	4.2325	0.047318	0.0076251	190.19	23.75	65.307	344.6	250.26	
XDT01-r13	0.0011172	0.00034339	0.069783	0.0027713	0.15295	0.0094809	0.020549	0.0063157	31.705	3.3356	0.053439	0.0062799	200.18	20.737	347.48	245.92	275.74	
XDT01-r14	0.00044319	0.00011739	0.055801	0.00083375	0.11946	0.002734	0.0081454	0.0021576	30.4	3.5239	0.049284	0.0020474	208.64	23.797	161.35	94.373	660.88	
XDT01-r15	0.0008627	0.00022056	0.059024	0.0024621	0.15164	0.012103	0.015861	0.0040551	30.96	3.037	0.04629	0.0043541	204.93	19.786	12.746	211.91	414.18	
XDT01-r2	0.00029677	9.25E-05	0.058239	0.0032122	0.10586	0.0046729	0.0054642	0.0017028	33.92	3.0737	0.0539	0.0035459	187.3	16.728	366.87	141.82	678.09	
XDT01-r3	0.0003567	0.00010971	0.054185	0.0017966	0.10289	0.0058006	0.0065618	0.0020182	32.046	1.4865	0.048937	0.0025089	198.08	9.0486	144.82	116.04	855.6	
XDT01-r4	0.00024233	7.36E-05	0.053497	0.0011844	0.085867	0.002185	0.0044556	0.0013524	31.158	1.44	0.049936	0.0016622	203.64	9.2644	192.02	75.63	1054.4	
XDT01-r5	0.0010987	0.00024144	0.071621	0.0024638	0.15393	0.011078	0.020229	0.0044451	33.746	1.9131	0.055591	0.0046744	188.25	10.518	436.07	177.05	322.32	
XDT01-r6	0.00014487	4.28E-05	0.053375	0.0025882	0.080471	0.0030471	0.0026642	0.0007866	31.559	2.1272	0.051249	0.0026808	201.1	13.346	252.07	116.07	1581.5	
XDT01-r7	0.00097693	0.0002838	0.070715	0.0052089	0.20787	0.016965	0.018001	0.0052293	35.647	4.3451	0.056478	0.0070281	178.35	21.442	471.22	254.01	189.24	
XDT01-r8	0.0014808	0.00049397	0.066169	0.0063419	0.15999	0.0071775	0.027261	0.0090939	33.618	4.067	0.044256	0.010456	188.96	22.527	1.11E-05	400.46	342.65	
XDT01-r9	0.00056562	0.00020279	0.057753	0.0011366	0.14278	0.0084031	0.010405	0.0037303	32.027	3.5349	0.049437	0.0034377	198.21	21.544	168.61	154.82	638.98	

c=core analysis, r- rim analysis

Table 1

Apatite SHRIMP analyses

	$^{238}U/^{206}Pb$	err	$^{207}Pb/^{206}Pb$	err	$^{204}Pb/^{206}Pb$	err	U ppm	^{206}Pb ppm	Pb ppm
DBT51-c1	16.182	1.067	0.42771	0.00980	0.03200	0.00273	8.8	0.47	0.685420019
DBT51-c2	47.668	8.291	0.26649	0.01575	0.01595	0.00191	46.7	0.85	1.087674141
DBT51-c3	62.403	6.114	0.35724	0.01424	0.01911	0.00211	29.4	0.41	0.561631341
DBT51-r01	10.712	15.006	0.54253	0.01619	0.03381	0.00686	5.6	0.45	0.715956502
DBT51-r02	25.282	2.030	0.33575	0.00573	0.01927	0.00253	14.8	0.51	0.684474298
DBT51-r03	20.151	0.914	0.38244	0.01001	0.02072	0.00250	9.3	0.40	0.561389484
DBT51-r04	5.125	0.333	0.39701	0.00700	0.02303	0.00205	5.4	0.91	1.286329034
DBT51-r05	14.016	0.663	0.38321	0.01219	0.02653	0.00225	7.1	0.44	0.619086882
DBT51-r06	19.520	0.604	0.33436	0.00692	0.02112	0.00150	15.0	0.66	0.900672473
DBT51-r07	18.883	0.824	0.35048	0.00947	0.01817	0.00168	12.1	0.55	0.759133745
DBT51-r08	19.826	2.153	0.37999	0.00906	0.02147	0.00221	12.0	0.53	0.735977769
DBT51-r09	45.372	1.507	0.25342	0.00733	0.01266	0.00173	27.2	0.52	0.656930411
DBT51-r10	19.017	0.948	0.35169	0.00822	0.02269	0.00202	9.2	0.42	0.572992349
DBT51-r11	24.870	1.446	0.32526	0.01258	0.01907	0.00194	11.0	0.38	0.514059878
DBT51-r12	21.049	0.864	0.32685	0.00939	0.01839	0.00233	12.9	0.53	0.711834804
DBT51-r13	42.045	4.136	0.25332	0.01613	0.01409	0.00293	26.4	0.54	0.690043008
DBT51-r14	16.188	3.304	0.40444	0.01366	0.02847	0.00364	4.8	0.26	0.369919529
DBT51-r15	12.800	1.219	0.34376	0.00686	0.02350	0.00215	6.4	0.43	0.591476676
DBT51-r16	16.903	1.300	0.32033	0.00640	0.02239	0.00288	8.1	0.41	0.556907791
DBT51-r17	20.778	1.176	0.32172	0.00705	0.02047	0.00192	11.8	0.49	0.657713366
DBT51-r18	17.640	1.013	0.35064	0.01071	0.01833	0.00364	7.0	0.34	0.469542677
DBT51-r19	12.874	4.250	0.31155	0.01312	0.02139	0.00324	6.4	0.43	0.569272869

Notes:

c= core analysis, r = rim analysis

Only rim data used for age estimate.

First rim datum measured under different conditions from others and excluded from age calculation

Table 2

Region	Rock type (Pluton	Sample	Location	
DANBA	granodiorite (DE	DBT-51	N31°08.98	E101°54.25'
	granite (DS)	DBA-27	N30°51.31	E101°49.20'
	granite (DS)	DBT-08	N30°54.76	E101°46.06'
	granite (GZ)	DBT-31	N30°45.11	E101°59.18'
	granite (GZ)	DBT-41	N30°47.61	E101°56.83'
	aplite (GZ)	DBW-19	N30°45.31	E101°58.93'
	pelitic schist	DBT63	N31°03.40	E101°52.05'
GONGASH	granite (ED)	EDT-02	N30°32.31	E101°37.06'
XINDUQIA	granodiotite (XD	XDT-01	N30°16.31	E101°31.15'
	granodiotite (JG	JGT-01	N29°53.71	E101°34.18'
	granodiotite (JG	JGT-02	N29°54.11	E101°34.77'
DAHEBIAN	granite (DHS)	DHT-04	N28°34.31	E101°44.18'
	granite (DHS)	DHT-05	N28°32.01	E101°44.90'
	granite (DHS)	DHT-09	N28°31.91	E101°44.88'
	granite (DHN)	DHT-03	N28°38.48	E101°38.67'

Table 3. Sample Locations